

Subject-Specific Finite Element Models of the Tibia With Realistic Boundary Conditions Predict Bending Deformations Consistent With In Vivo Measurement

Ifaz T. Haider¹

Human Performance Laboratory,
Faculty of Kinesiology and the
McCaig Institute for Bone and Joint Health,
University of Calgary,
2500 University Dr. NW,
Calgary, AB T2N 1N4, Canada
e-mail: ifaz.haider@ucalgary.ca

Michael Baggaley

Human Performance Laboratory,
Faculty of Kinesiology and the
McCaig Institute for Bone and Joint Health,
University of Calgary,
2500 University Dr. NW,
Calgary, AB T2N 1N4, Canada
e-mail: michael.baggaley1@ucalgary.ca

W. Brent Edwards

Human Performance Laboratory,
Faculty of Kinesiology and the
McCaig Institute for Bone and Joint Health,
University of Calgary,
2500 University Dr. NW,
Calgary, AB T2N 1N4, Canada
e-mail: wbedward@ucalgary.ca

Understanding the structural response of bone during locomotion may help understand the etiology of stress fracture. This can be done in a subject-specific manner using finite element (FE) modeling, but care is needed to ensure that modeling assumptions reflect the in vivo environment. Here, we explored the influence of loading and boundary conditions (BC), and compared predictions to previous in vivo measurements. Data were collected from a female participant who walked/ran on an instrumented treadmill while motion data were captured. Inverse dynamics of the leg (foot, shank, and thigh segments) was combined with a musculoskeletal (MSK) model to estimate muscle and joint contact forces. These forces were applied to an FE model of the tibia, generated from computed tomography (CT). Eight conditions varying loading/BCs were investigated. We found that modeling the fibula was necessary to predict realistic tibia bending. Applying joint moments from the MSK model to the FE model was also needed to predict torsional deformation. During walking, the most complex model predicted deformation of 0.5 deg posterior, 0.8 deg medial, and 1.4 deg internal rotation, comparable to in vivo measurements of 0.5–1 deg, 0.15–0.7 deg, and 0.75–2.2 deg, respectively. During running, predicted deformations of 0.3 deg posterior, 0.3 deg medial, and 0.5 deg internal rotation somewhat underestimated in vivo measures of 0.85–1.9 deg, 0.3–0.9 deg, 0.65–1.72 deg, respectively. Overall, these models may be sufficiently realistic to be used in future investigations of tibial stress fracture. [DOI: 10.1115/1.4044034]

1 Introduction

Stress fractures of the tibia are a common overuse injury among active individuals [1,2]. These fractures are believed to be associated with mechanical fatigue [3,4], wherein repetitive submaximal loading results in progressive microcrack accumulation, degradation of material properties, and eventual fracture [5,6]. This process can be insidious, and occur in otherwise healthy bone [7], making injuries difficult to predict. However, it is well understood that the damage accumulation rate and fatigue life of bone, at the material level, are strongly related to stress and strain magnitude [6,8]. Thus, understanding the mechanical response of the tibia to physical activity may be the key to understanding the etiology of these injuries.

Previous studies have measured tibial strains in vivo using surgically implanted instrumented strain gauges [9–13]. Strains were measured during a multitude of activities, including walking, running, and jumping under different terrain and fatigue conditions. However, measurements were limited by the fact that strain gauges can only be placed in a small number of easily accessible locations; these locations may not be sites critical to stress fracture. Alternatively, Yang et al. [14] measured tibial deformations in vivo using surgically implanted bone pins. Unlike localized measures from strain gauges, this technique provides a measure of the overall mechanical response of the whole bone, though it is challenging to relate these results to material strain. In either case,

both of these techniques require invasive surgery, making them unsuitable for larger studies.

Computer modeling may overcome this limitation. Our group utilizes an inverse-dynamics approach, where musculoskeletal (MSK) modeling is used to estimate loads during locomotion based on motion capture and ground reaction force data. The loads are then applied to subject-specific computed tomography (CT)-based finite element (FE) models for noninvasive estimation of bone deformation [15–17]. As with all modeling approaches, care must be taken to ensure that model assumptions accurately reflect the reality of interest. The mechanical environment of the tibia is complex, dependent among other things on muscles, bone-on-bone contact, and constraining ligaments. In recent literature, we found a number of FE studies that modeled tibial deformation during locomotion that used different schemes for loads and constraints [16,18–20]. The influence that these different choices have on results from FE simulations remains unclear, as does their ability to accurately represent the in vivo condition.

The purpose of this study was to assess the sensitivity of different boundary constraint (BC) and loading conditions for FE models of the tibia in locomotion. We hypothesized that previously utilized modeling conditions oversimplified the loading environment of the tibia, resulting in physiologically unrealistic predictions of deformation. To test this hypothesis, we used subject-specific FE models to predict tibial deformation during walking at four fixed speeds and running at one fixed speed. We developed multiple models, progressively increasing the complexity of loads and BCs; predictions from these models were then compared to deformations measured in vivo using bone pins [14].

¹Corresponding author.

Manuscript received October 12, 2018; final manuscript received May 30, 2019; published online October 11, 2019. Assoc. Editor: Guy Genin.

2 Methods

2.1 Motion Capture and Musculoskeletal Modeling.

Motion capture data were collected from a young female participant (age = 22 years, mass = 56 kg, height = 170 cm). Twenty-four retroreflective markers were placed on the pelvis and right lower limb. The participant was instructed to walk on an instrumented treadmill (Bertec, Columbus, OH) at four fixed speeds (2.5 km/h, 3.5 km/h, 4.5 km/h and 5.5 km/h) and run at one fixed speed (5.5 km/h). Motion and force data were concurrently captured at 200 Hz and 1000 Hz, respectively, using a VICON NEXUS motion capture system (software v. 1.8.4, Vicon Motion Systems Ltd, Oxford, UK).

Lower extremity muscle and joint contact forces during locomotion were estimated with inverse dynamics-based static optimization, using an approach that was conceptually similar to our previous work [16]. Segment weights, centers of mass, and moments of inertia for inverse dynamics analysis were calculated using the equations of Vaughan et al. [21]. A musculoskeletal model, previously reported in greater detail [22], was implemented in MATLAB (MathWorks, Natick, MA) and used to obtain muscle moment arms, muscle orientations, and maximal dynamic muscle forces. Initial geometry and muscle parameters were obtained from Arnold et al. [23], which were then scaled according to the participant's mass and segment lengths. Muscle moment arms were computed at each frame by first orienting all segments into the position obtained from motion capture, and then perturbing joint angles by ± 10 deg. The moment arm of each muscle was calculated from the change in muscle length divided by the change in joint angle. Maximal dynamic muscle forces were computed for each muscle, at every frame, which served as upper bounds for the static optimization routine described below. An active force adjustment (F_a), passive force adjustment (F_p), and velocity adjustment (F_v) term was computed by interpolating curves from Arnold et al. [23] as a function of fiber length and velocity. These parameters were then used to calculate maximal dynamic muscle force based on the muscles' maximal isometric muscle force

$$\text{MDMF} = (F_a \cdot F_v) \cdot \text{MIMF} + F_p \cdot \text{MIMF} \quad (1)$$

where MDMF is the maximal dynamic muscle force for a given muscle, and MIMF is the corresponding muscles' maximal isometric muscle force. Information from the MSK model were used in a static optimization routine to estimate muscle forces. The optimization was solved with the interior point algorithm from the MATLAB Optimization Toolkit (MathWorks, Natick, MA). Forces were computed such that the sum of muscle moments at each joint was equal to the joint moment at all active constraints. Five moments were used for constraints including: flexion–extension and adduction–abduction moments at the hip, flexion–extension moment at the knee, flexion–extension moment at the ankle, and subtalar moment. Under-constraint of the solution space was resolved by accepting the answer that minimized the sum of muscle stresses squared. Joint contact forces were then computed using Eq. (2)

$$\mathbf{JRF} = \sum_{i=1}^N \mathbf{MF}_i + \mathbf{JCF} \quad (2)$$

Where \mathbf{JRF} is the joint reaction force computed from inverse dynamics, \mathbf{JCF} is the joint (bone-on-bone) contact force, \mathbf{MF}_i is the force vector of the i th muscle that crosses the joint, and N is the total number of muscles that cross the joint.

2.2 Finite Element Modeling. Forces and moments from the MSK model were applied to a subject-specific FE model generated from CT scans of the participant's left leg. Scans were acquired using a GE Revolution GSI (GE Healthcare) with image

acquisition settings of 120 kVp, and 180 mA. Images were reconstructed with an in-plane resolution of $0.486 \text{ mm} \times 0.486 \text{ mm}$ and a slice thickness of 0.625 mm. A hydroxyapatite calibration phantom (QRM GmbH; Möhrendorf, Germany) in the field-of-view was used to identify a linear relationship between CT intensity measured in Hounsfield units and equivalent bone mineral density (ρ_{HU} ; g/cm^3). Image analysis and mesh generation was performed using the Mimics Innovation Suite (v19, Materialize, Leuven, Belgium). A threshold of 0.15 g/cm^3 was used to identify the periosteal surface of bone. Bones were meshed with quadratic tetrahedral elements with an average element edge length of 2.0 mm, resulting in a 220,000 element mesh of the tibia and 60,000 element mesh of the fibula. A sensitivity test revealed that increasing the number of elements by 50% changed surface strains by less than 1%, suggesting that the mesh was adequately converged

Bone was modeled as an inhomogeneous, orthotropic material [24]. Each element was assigned an elastic constant based on bone apparent density (ρ_{app})

$$E_3 = 6570 \cdot \rho_{\text{app}}^{1.37} \quad (3)$$

where E_3 is the elastic modulus (MPa) of bone in the axial direction and ρ_{app} for each element volume was equal to $\rho_{\text{HU}}/0.626$; g/cm^3 [25]. The other elastic constants were obtained assuming constant anisotropy throughout: $E_1 = 0.574 \cdot E_3$, $E_2 = 0.577 \cdot E_3$, $G_{12} = 0.195 \cdot E_3$, $G_{23} = 0.265 \cdot E_3$, $G_{31} = 0.216 \cdot E_3$, $\nu_{12} = 0.427$, $\nu_{23} = 0.234$, and $\nu_{31} = 0.405$ [26]. Here, subscripts 1–3 denote the medial–lateral, anterior–posterior, and axial directions, respectively. These anisotropic definitions illustrated excellent agreement between experimentally measured and FE predicted principal strains for a cadaveric tibia loaded in axial compression ($r^2 \geq 0.97$; error $\leq 8.8\%$) and torsion ($r^2 = 0.99$; error = 6.3%) (Gray et al. 2008).

2.2.1 FE Boundary Constraints. Similar to other studies in the literature [19], we first chose to use a simple fixed constraint (FC) at the distal tibia, where surface nodes near the tibia–talus interface (Fig. 1; left) were fully constrained in translation and rotation. We also examined a more realistic pinned constraint (PC) condition, similar to what Speirs et al. [27] suggested for the femur. In this condition, the ankle center of rotation was estimated as the midpoint between the malleoli. Surface nodes near the tibia–talus interface were kinematically coupled to rotate about this fixed point. One point on the medial malleolus was constrained in the anterior–posterior direction, and one point on the tibial plateau was fixed in the anterior–posterior and medial–lateral directions. This same point on the tibial plateau was used for the application of contact force, discussed in the Sec. 2.2.2.

2.2.2 FE Loading Conditions. The knee joint contact force, computed from the MSK model (Eq. (2)) was applied to all FE models. Load was modeled as a concentrated force applied to a single node on the tibial plateau, located at the center of pressure as identified from a previous study using telemetric implants [28]. Many previous FE studies also explicitly modeled individual muscle forces [18–20]. Muscle insertion points were identified by aligning the MSK model geometry and FE mesh using an iterative closest point algorithm (CLOUDCOMPARE software, open source²). After alignment, each muscle attachment node from the MSK model was mapped to the nearest surface node of the FE mesh, and a concentrated force was applied at each attachment point. The following muscles were included in the FE model: the semi-membranosus, semitendinosus, bicep femoris (long and short heads), sartorius, tensor fasciae latae, gracilis, soleus, tibialis posterior, tibialis anterior, flexor digitorum, flexor hallucis, peroneus brevis, peroneus longus, peroneus tertius, and extensor digitorum. Patellar ligament force was also included in the FE model.

²<http://www.danielgm.net/cc/>

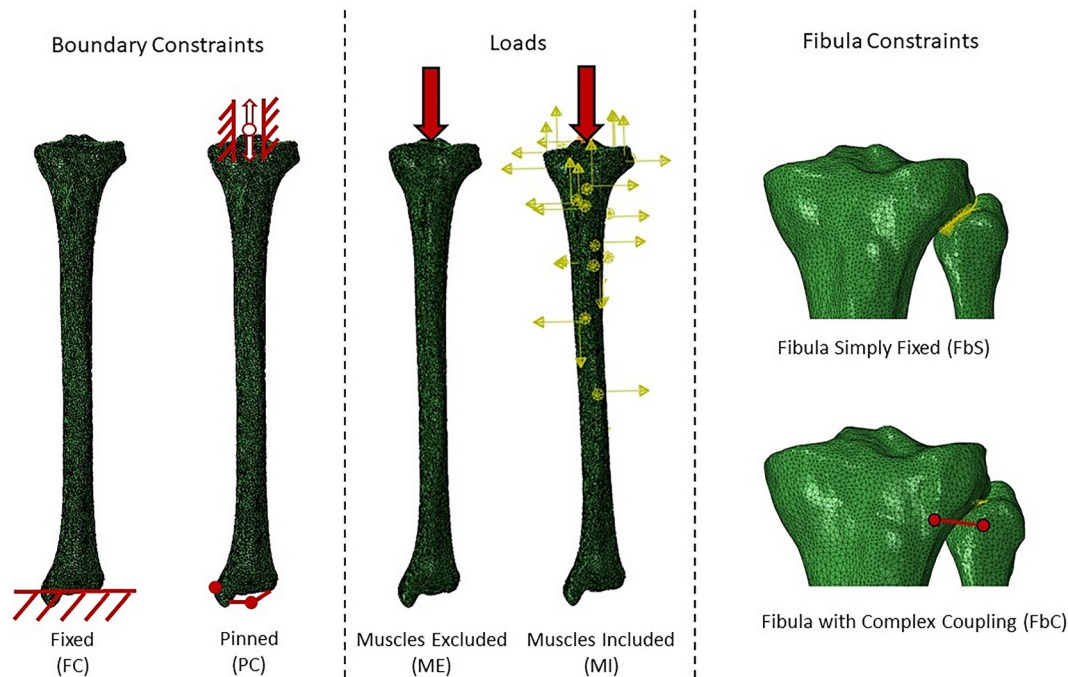


Fig. 1 Summary of model conditions. left: Models used either a fully FC, where the distal end was fully restricted from translation and rotation or a PC where the distal end was free to rotate about the ankle center. middle: Some models were simulated with a contact force only, with muscles excluded (ME), other models were simulated with all muscle forces explicated modeled (MI). right: Some models were simulated a fibula excluded (FbN; not shown). Other models used a simple constraint for the proximal tibiofibular joint (FbS). A final case used spring elements to simulate anterior (lighter line/red line) and posterior (not shown) ligament complexes holding these bones together (FbC).

Regardless of whether we included (MI condition) or excluded muscles (ME condition), FE models were simulated during both peaks of vertical ground reaction force in walking and at peak vertical ground reaction force in running.

2.2.3 Tibia-Fibula Interactions. We originally simulated geometry of the tibia only (FbE condition), with the fibula excluded [16,18]. We also had conditions to explore the mechanical contribution of the fibula. For this, it was necessary to make assumptions about how the tibia and fibula interact at their shared joints. We initially assumed a simple constraint with rigid joints [20,29], modeled with surface-based tie constraints in ABAQUS (FbS condition; Fig. 1). However, the proximal tibiofibular joint, in particular, is known to accommodate some relative motion during movement [30,31]. We simulated this motion using a more complex constraint, with spring elements to model the anterior and posterior ligament complexes. Nodes at the articulating surface were then tied in the direction normal to the joint surface, preventing unrealistic penetration or joint opening while still allowing relative sliding motion. Two different conditions were generated with complex tibia-fibular constraints. One condition used the complex constraint on the proximal joint only, while the distal joint remained simply constrained (FbC condition; Fig. 1). Another condition applied complex constraints to both the proximal and distal tibia-fibular joints (FbCC condition). In both conditions, the stiffness of each ligament complex was based on previously published values: 133 N/mm at the proximal anterior, and 109 N/mm at the proximal posterior, 78 N/mm at the distal anterior, and 101 N/mm at the distal posterior [32,33].

2.2.4 Applied Moments. The MSK model predicts nontrivial joint moments at both the ankle and knee. Joint moment is the net of actions from all sources (muscle, bone-on-bone contact, ligaments) and is required to maintain dynamic equilibrium of the body segment. FE models that include muscle forces are able to

capture some, but not all, of the contributions to the joint moment. We postulate the following relationship at the knee:

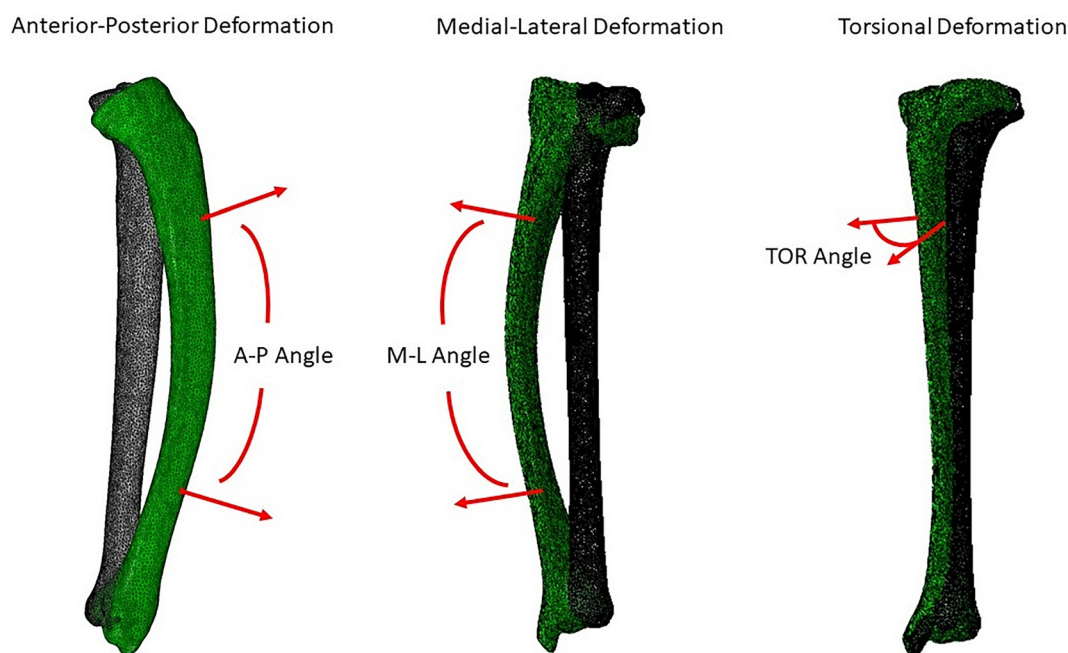
$$\mathbf{JM}_{\text{knee}} = \sum_{i=1}^9 (\mathbf{r}_{i-\text{knee}} \times \mathbf{MF}_{i-\text{knee}}) + \mathbf{ResM}_{\text{knee}} \quad (4)$$

where $\mathbf{JM}_{\text{knee}}$ is the joint moment at the knee, computed from the MSK model. \mathbf{MF}_i and \mathbf{r}_i are the respective force and moment arm of the i th of nine muscles crossing the knee that also have an insertion point on the tibia. $\mathbf{ResM}_{\text{knee}}$ is a residual moment term that accounts for all other sources of moment about the knee. There are two major reasons why this term exists. First, biarticulating muscles such as the gastrocnemius do not have insertion points on the tibia, but can still generate moments about the knee. Second, as noted in Sec. 2.1, torsional moment about the knee is not an active constraint in the calculation of muscle forces at the knee. This is likely the correct approach, given that engaging muscles at the knee alone generates little internal-external rotation of the lower leg. The torsional component of knee joint moment is likely generated by muscles and movements on other parts of the body and transmitted to the tibia through ligaments and bone-on-bone contact. We hypothesized that FE predictions would be more accurate if we apply $\mathbf{ResM}_{\text{knee}}$ as a couple moment to the proximal tibia, referred to as the moment enhanced (MoE) condition.

2.3 Model Conditions and Variables of Interest. Different model conditions were generated by varying locomotion, boundary constraints, loading conditions, tibia-fibula interactions, and applied moments. Nine different model conditions of increasing complexity were developed to simulate walking, and another four different models to simulate running. Details of these conditions are shown in Table 1.

Table 1 Summary of simulation cases

Model condition	BC	Muscles	Fibula	Locomotion	Gait manipulation	Moment enhancement
FC-ME-FbE	Fixed	Excluded	Excluded	Walking + running	None	No
FC-MI-FbE	Fixed	Included	Excluded	Walking + running	None	No
PC-MI-FbE	Pinned	Included	Excluded	Walking + running	None	No
PC-MI-FbS	Pinned	Included	Simple distal joint Simple proximal joint	Walking	None	No
PC-MI-FbC	Pinned	Included	Simple distal joint Complex proximal joint	Walking	None	No
PC-MI-FbCC	Pinned	Included	Complex distal joint Complex proximal joint	Walking	None	No
PC-MI-FbC-Pr	Pinned	Included	Simple distal joint Complex proximal joint	Walking	Exaggerated pronation	No
PC-MI-FbC-MoE	Pinned	Included	Simple distal joint Complex proximal joint	Walking + Running	None	Yes
PC-MI-FbC-MoE-Pr	Pinned	Included	Simple distal joint Complex proximal joint	Walking	Exaggerated pronation	Yes

**Fig. 2 Example of tibia deformations. The unloaded tibia (gray) can bend in the anterior-posterior direction (left), medial-lateral direction (middle) or in torsion (right).**

Deformation predicted by each model was compared to measurements reported by Yang et al. [14]. In their study, bone pins were surgically implanted 10 cm below the tibial plateau and 10 cm above the medial malleolus. Deformation angles were reported as the change in relative angle between the two pins during loading. We replicated this in simulation by measuring the angle between surface normal at the two locations and reported deformation as the change in angle after loading. We reported bending about the anterior–posterior (A-P), medial–lateral (M-L) and torsional axes (Fig. 2). Model predictions were compared to the in vivo measurements and linear regression analysis in SPSS (v24, IBM, Armonk, NY) was used to examine the relationship between walking speed and deformation angle. Finally, model predicted strains were compared to strains previously reported from in vivo measurements [12,13]. A surface element on the medial midshaft, i.e., a best estimate of the strain gauge location in these two reference studies, was identified, and the minimum and maximum principal strains at this location were reported. To

account for errors in site selection, the highest and lowest magnitude principle strains within a 5 mm radius of this point were also reported.

3 Results

The different model conditions (Table 1) produced very different predictions of deformation angle during walking (Fig. 3; top). At a 4.5 km/h walking speed, Yang et al. [14] measured A-P deformation of 0.5–1 deg (posterior), M-L deformation of 0.15–0.7 deg (medial), and torsional deformation of 0.75–2.2 deg (internal rotation). Model conditions FC-ME-FbE, FC-MI-FbE, and PC-MI-FbE, which did not have a fibula, predicted A-P and M-L deformations between 1.9–8.7 deg and –13 deg to 2.8 deg, respectively. These values are exceptionally large and/or in the opposite direction compared to in vivo measurements. Adding the fibula attenuated predictions to more comparable levels, but the magnitude of attenuation was somewhat dependent on how the

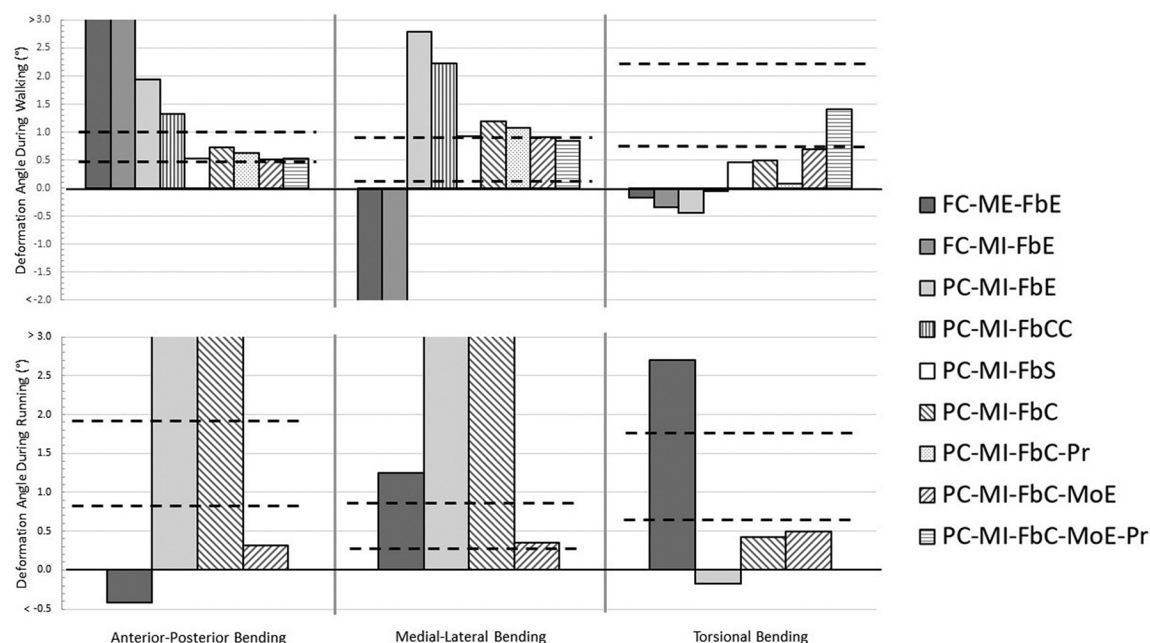


Fig. 3 Peak deformation angles during walking at 4.5 km/h (top) and running at 5.5 km/h (bottom). Dotted lines indicate the range of values from in vivo measurements. Deformation in the posterior, medial, and internal rotation directions is defined as positive; examples of these deformations are shown in Fig. 2.

tibia-fibula interactions were modeled. The PC-MI-FbS condition predicted the most rigid structure, with A-P and M-L deformation of 0.5 deg and 0.9 deg, respectively, while the PC-MI-FbC condition produced slightly greater deformations of 0.7 deg and 1.2 deg, respectively. Finally, the PC-MI-FbCC condition produced deformations of 1.3 deg and 2.2 deg, similar to a model with no fibula at all (PC-MI-FE). As described in more detail in the discussion, this condition may be underconstrained.

All of these conditions predicted torsional deformations much lower than in vivo measures, however. This changed when we simulated the moment enhancement condition. Compared to PC-MI-FbC, the PC-MI-FbC-MoE condition experienced an elevated torsional deformation of 0.70 deg, just below the in vivo measure. Instructing the participant to walk with exaggerated pronation further increased torsional deformation to 1.4 deg, while leaving the other two deformation angles relatively unchanged.

The different model conditions also predicted very different deformation angles during running (Fig. 3; bottom). In vivo measurements were between 0.85–1.9 deg in posterior bending, 0.3–0.9 deg in medial bending, and 0.65–1.72 deg in internal rotation [14]. Again, the simpler model conditions either overestimated deformation or predicted deformation in the wrong direction, with A-P deformation angles of -0.48 deg to 8.1 deg and M-L deformation angles of 1.2 deg to 10.8 deg. The most complex model condition, PC-MI-FbC-MoE produced results most similar to in vivo measurements. However, A-P bending and torsion was still somewhat lower than measurements, with deformation angles of 0.32 deg and 0.5 deg, respectively.

Figure 4 (left) shows the strain distribution predicted for the PC-MI-FbC-MoE condition during walking at 4.5 km/h and running at 5.5 km/h. At the medial midshaft, the model predicted a maximum principal strain of $490 \mu\epsilon$ (min: 420 ; max: $529 \mu\epsilon$) and a minimum principal strain of $-570 \mu\epsilon$ (min magnitude: $-440 \mu\epsilon$; max magnitude: $-680 \mu\epsilon$). However, strains were elevated along the posterior aspect of the tibia, near the midshaft. Here, the model predicted maximum and minimum principal strains of $1500 \mu\epsilon$ and $-2400 \mu\epsilon$, respectively. Higher strains were also predicted when the same model condition was used to simulate running (Fig. 4; right), with a maximum principal strain of 579 (min: $345 \mu\epsilon$; max: $781 \mu\epsilon$) and minimum principal strain of $-770 \mu\epsilon$

(min magnitude: $-445 \mu\epsilon$; max magnitude: $-1120 \mu\epsilon$) at the medial midshaft. In this model, strains were elevated along the lateral midshaft (max principal: $3200 \mu\epsilon$, min principal: $-3700 \mu\epsilon$).

Figure 5 shows the relationship between walking speed and predicted deformation, for the PC-MI-FbC-MoE condition. Between 3.5 and 5.5 km/h, there was a strong linear regression relationship between walking speed and A-P deformation ($p = 0.045$, $R^2 = 0.995$), and no significant relationship between speed and the other two deformation angles ($p > 0.60$). However, these trends do not hold if we consider the 2.5 km/h walking condition. Potential reasons for this deviation in behavior are detailed in the discussion.

Speed and walking/running condition was also associated with changes to forces and moments. In general, the peak forces were lowest during walking at 2.5 km/h and increased steadily with walking speed; the maximum peak force typically occurred during running (Fig. 6). With this pattern in mind, the first of peak of vertical ground reaction force varied between 1.03 times bodyweight (BW) during 2.5 km/h walking, and 2.30 BW during 5.5 km/h running. The second peak of vertical ground reaction force was somewhat less affected by walking speed, with forces between 0.999 and 1.06 BW for walking at 2.5 km/h and 5.5 km/h, respectively. Finally, predicted axial knee contact force varied between 3.42 BW during walking at 2.5 km/h, to 8.47 BW during running at 5.5 km/h. Joint moments followed a similar pattern, with the lowest peak moments during 2.5 km/h walking and the greatest moments during 5.5 km/h running (Fig. 7).

4 Discussion

The purpose of this study was to assess the sensitivity of subject-specific FE analysis under different BC and loading conditions. The simplest model conditions generated tibial deformations that did not agree with previously reported in vivo measurements [14]. However, our most complex models, PC-MI-FbC-MoE and PC-MI-FbC-MoE-Pr, were able to predict tibial deformations more comparable to these measures.

Previous studies have performed FE simulations with [20] and without [16,18] a fibula. To our knowledge, however, no studies have investigated how inclusion of the fibula may influence the structural response of the tibia during locomotion. In this study,

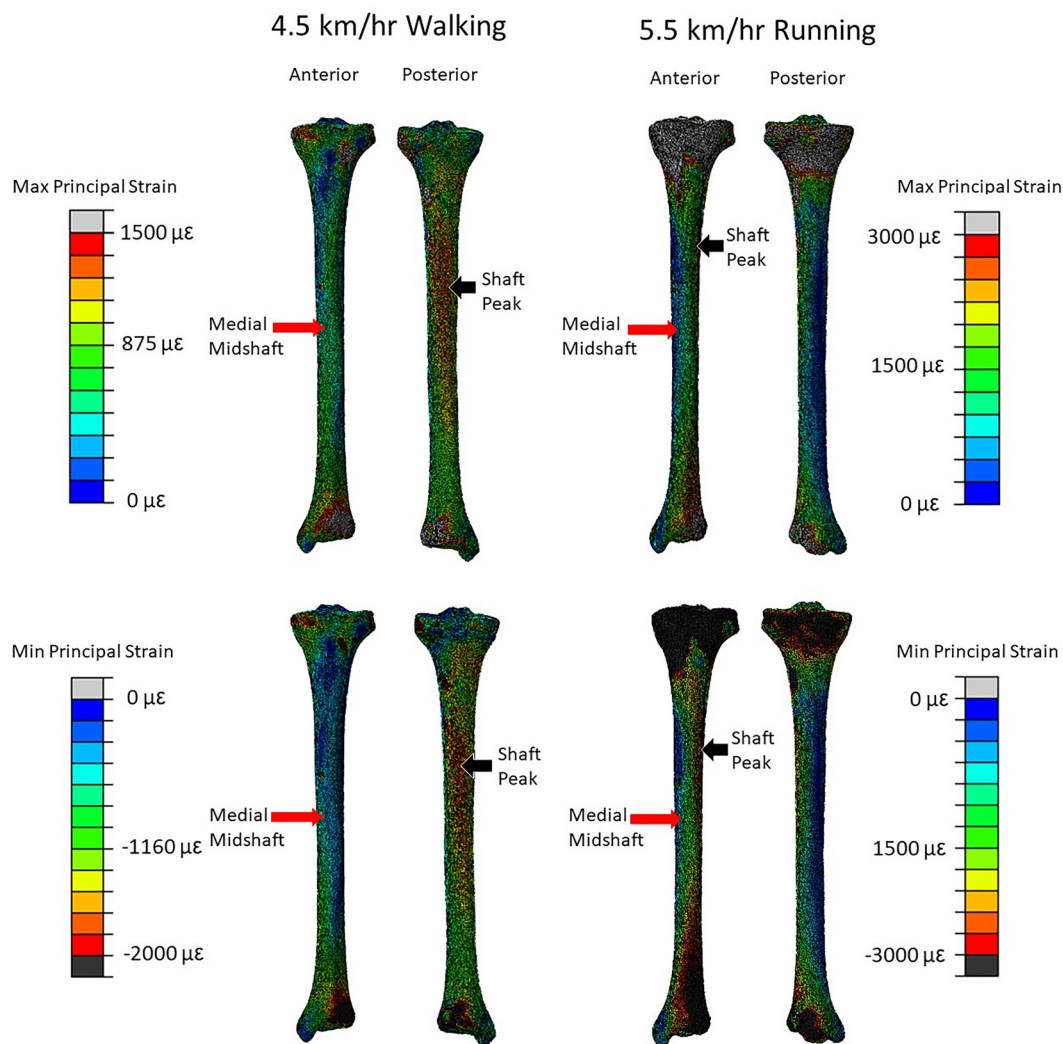


Fig. 4 Maximum principal strain (top) and minimum principal strain (bottom) of the tibia in the PC-MI-FbC-MoE condition during walking at 4.5 km/h (left) and running at 5.5 km/h (right). Locations of peak shaft strains are indicated with a black arrow.

we found that FE models without a fibula illustrated large bending angles in the A-P and M-L directions. Including the fibula resulted in deformation predictions closer to in vivo measures. In addition to having some compressive load bearing capacity [34], these data suggest that the fibula functions as a structural brace, restricting medial and posterior motion of the plateau relative to the malleoli.

The influence of the fibula was somewhat dependent on how the tibia-fibula interaction was modeled. The PC-MI-FbS condition, with simple constraints on the proximal and distal end, and the PC-MI-FbC condition, with simple constraint on the distal end and a complex constraint on the proximal end, both predicted A-P and M-L deformation comparable to in vivo measures [14]. However, a fibula model with complex constraint at both proximal and distal ends (Fig. 3; case PC-MI-FbCC) predicted large deformation angles, more similar to a model with no fibula at all. We postulate that it is unrealistic to apply the complex constraint condition to the distal joint. Unlike the proximal tibiofibular joint, which has few ligament attachments, the distal tibiofibular joint is constricted by the ankle joint capsule, which includes the constraining geometry of the talus and attachment to many other bones of the foot. It may be possible to produce a more accurate representation of the ankle joint by including all relevant bones and ligaments. However, this would significantly increase model complexity and was not explored further in this work.

Our initial BC and loading conditions were based off of previously published work [16,19,20,35], but even the more complex

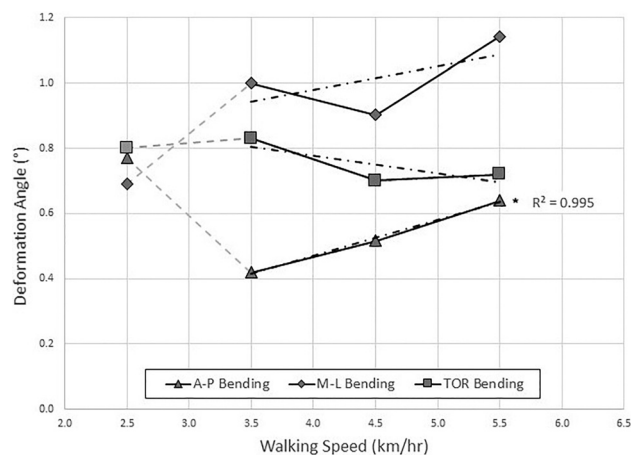


Fig. 5 Changes in peak deformation for the PC-MI-FbC-MoE condition as a function of walking speed. Between 3.5 and 5.5 km/h, there was a significant linear regression relationship between A-P deformation angle and walking speed ($p = 0.045$; $R^2 = 0.995$), with no significant relationship for the other two deformation angles.

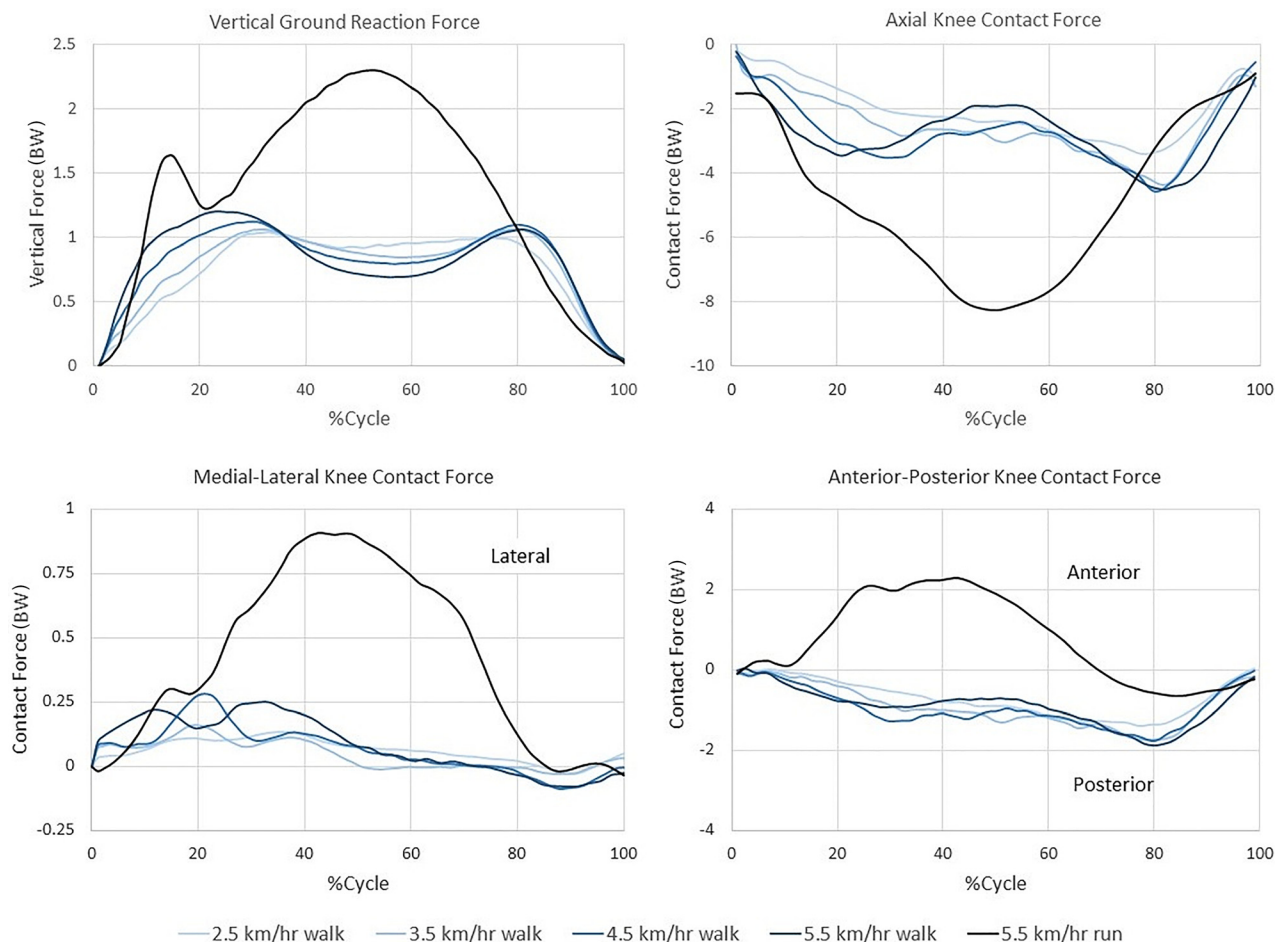


Fig. 6 Vertical ground reaction force (top left), axial knee contact force (top right), medial-lateral knee contact force (bottom left), and anterior-posterior knee contact force (bottom right), across all walking and running conditions

conditions (PC-MI-FbS and PC-MI-FbC) underestimated torsional deformation during walking. We noted that muscle forces in the FE model did not fully account for the joint moments predicted by the MSK model, and thus calculated a residual moment term (Eq. (4)) to model contributions from sources that are not explicitly part of the simulation. Adding the residual moment (MoE condition) increased torsional deformation, resulting in values more similar to in vivo measurement. The MoE condition also had a significant impact on FE simulations during running. Here, the other three conditions predicted very large deformations. These were attenuated in the PC-MI-FbC-MoE condition, and these results were again more similar to in vivo measurements. While this condition predicts A-P deformation lower than in vivo measures, we believe that the MoE condition provides a more realistic structural response, which may be required to provide meaningful assessments of stress fracture risk in runners [16,36,37].

Indeed, the PC-MI-FbC-MoE condition produced patterns of strain that are consistent with literature. Using in vivo strain measurement techniques, Lanyon et al. [13] reported peak maximum and minimum principal strains of $395 \mu\epsilon$ and $-434 \mu\epsilon$, respectively, in a 35 year-old male during treadmill walking at 5 km/h. Similarly, Burr et al. [12] reported maximum and minimum strains of $437 \mu\epsilon$ and $-544 \mu\epsilon$, in males during overground walking at 5 km/h. These values compare favorably to our model predictions of maximum principal strain (420 – $529 \mu\epsilon$), and minimum principal strain ($-400 \mu\epsilon$ to $-680 \mu\epsilon$). Lanyon et al. [13] also reported strains during treadmill running at 7.9 km/h, while Burr et al. [12] reported strains during overground jogging at 10.2 km/h. Respectively, these studies reported maximum principal strains of $625 \mu\epsilon$ and $746 \mu\epsilon$, and minimum principal strains of

$-879 \mu\epsilon$ and $-450 \mu\epsilon$. Again, these values are comparable to our model predictions of maximum (345 – $781 \mu\epsilon$) and minimum ($-445 \mu\epsilon$ to $-1120 \mu\epsilon$) principal strain during treadmill running at 5.5 km/h. It should be noted, however, that the running speed in this study was much lower than these two referenced studies. There may also be differences due to subject demographics, i.e., young female versus middle-age male.

When walking naturally, our participant generated vertical ground reaction forces that were consistent with in vivo measurements by Yang et al. [14], but vertical free moments (VFM) were an order of magnitude lower [14]. This was a plausible result, as previous studies have also observed large differences in VFM between participants [38]. However, we speculated that this could cause differences between our results and the deformations reported by Yang et al. [14]. Therefore, the participant was also instructed to walk with exaggerated foot pronation, as this change was likely to increase VFM during walking [39]. The strategy was effective; VFM increased by 20% and torsional deformation of the model increased from 0.7 deg to 1.4 deg, while deformation in the other two directions remained largely unchanged. Though limited to a single participant, these data provide preliminary indications that changes to gait can have a large impact on torsional deformation of the tibia, and this could have important clinical implications. Torsional deformation is associated with VFM [14], which in turn has been retrospectively linked to stress fracture [38]. While data are limited, there are also indications that some stress fractures can illustrate a spiral pattern [40] further implicating torsion as potentially important failure mode.

This study also explored how tibia deformation changed as a function of walking speed. At speeds between 3.5 and 5.5 km/h,

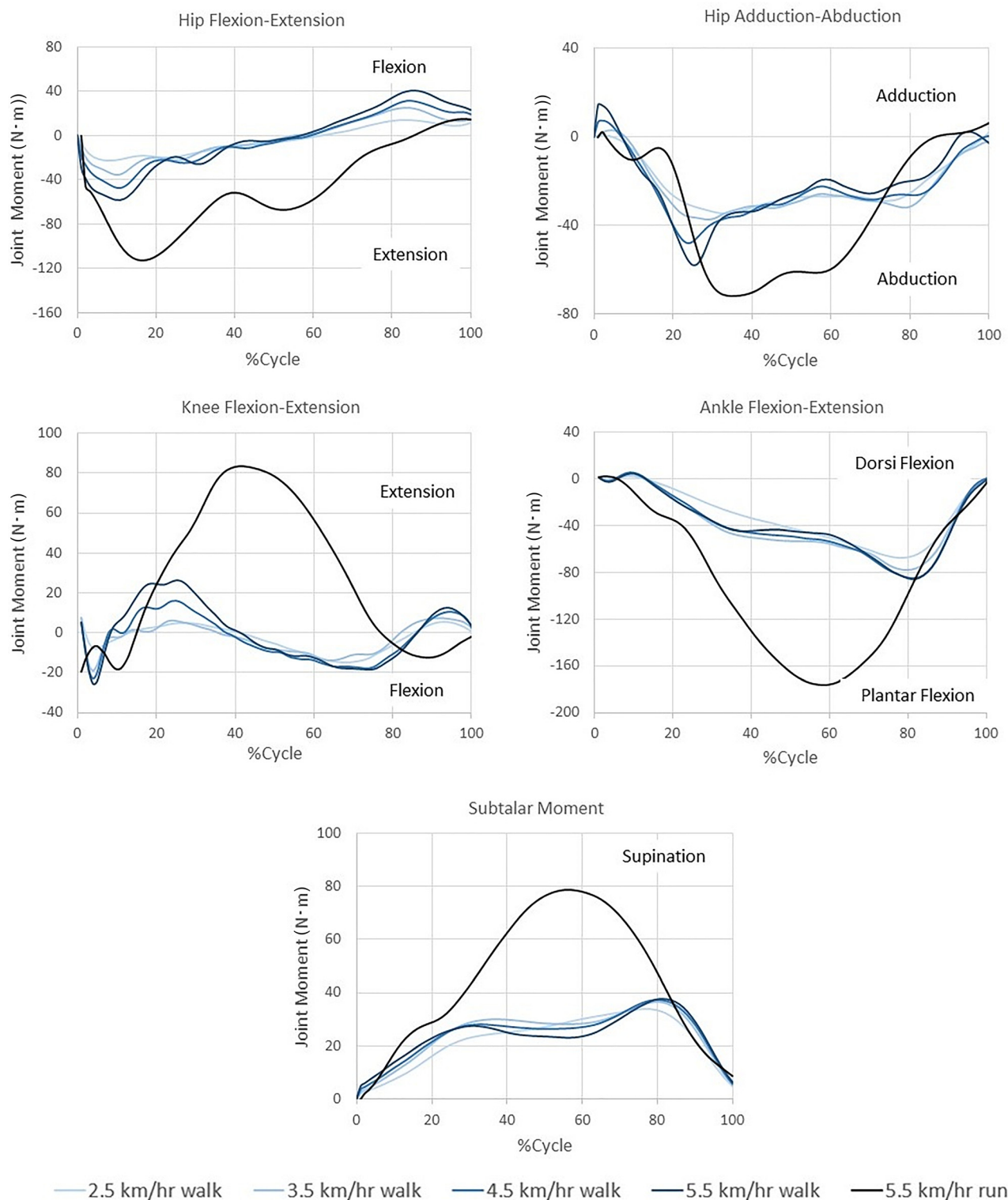


Fig. 7 Predicted joint moments during walking at four speeds (2.5 km/h, 3.5 km/h, 4.5 km/h, 5.5 km/h) and running at 5.5 km/h. All five of the moments shown here were used to constrain the static optimization routine that predicted muscle forces during walking and gait.

there was a strong linear relationship between walking speed and A-P deformation, but no relationship between walking speed in M-L or torsional deformation. These trends are comparable to findings by Yang et al. [14]; all of their participants experienced statistically significant increases in A-P deformation with increased speed, but M-L and torsional deformation could trend in either direction for a given individual and were rarely significant.

In this study, however, the relationship between walking speed and A-P deformation does not hold if we also consider results from the 2.5 km/h walking condition (Fig. 4). During data collection, the participant noted that this walking speed felt uncomfortably slow compared to her preferred gait. This was not surprising, as the average preferred treadmill walking speed is approximately 4.2 km/h [41]. We speculate that the participant may have made

significant changes to walking strategy in order to achieve a pace that was unusual for her, which may have influenced the results at this speed. Indeed, simulation results showed some important differences during walking at 2.5 km/h compared to 3.5 km/h. During the first peak of ground reaction force, subtalar pronation angle was 17% smaller at the slower speed. This caused noticeable changes to the instantaneous moment arms of the muscles associated with subtalar motion (-15% to $+10\%$, varying across the muscles), which influenced how muscle forces were distributed during walking. As a result, the model predicted a large elevation in force at the tibialis posterior at 2.5 km/h compared to 3.5 km/h, despite the fact that joint moments were not greater at the slower speed (Fig. 7). Due to its location near the proximal tibia, it is likely that the increased force contributed to compression-induced bending of the tibia, resulting in elevated A-P deformation at this speed.

One important limitation of this work is that we were unable to directly validate joint contact forces and muscle forces predicted using inverse dynamics combined with MSK modeling, as these forces are challenging to measure during locomotion in vivo. Indirect comparisons, however, suggest the general validity of the approach used in this work. The model used here predicted knee contact forces of 3.4–4.5 BW for treadmill walking between 2.5 and 5.5 km/h. This was compared favorably to contact force data from telemetric hip implants, where axial knee contact forces between 2.3 and 3.2 BW were recorded during treadmill walking at 4.0 km/h [42], noting that an implanted individual may walk differently compared to the healthy subject in this study. Moreover, the integrative MSK-FE modeling approach used in this work was able to predict deformation angles and strains consistent with in vivo measurement, further suggesting the validity of the muscle and contact forces used as input to the FE model. The MSK model in this study was also used alongside subject-specific FE in the past, to generate strain predictions consistent with in vivo measures [43].

This study has a few other noteworthy limitations. First, we did not have subject-specific in vivo measurements of deformation for our participant, and instead compared FE models to previously reported results. We were unable to compute precise error values for each simulation, but comparisons to previously reported measurements helped identify conditions where deformations appeared unrealistic. Second, even the more complex constraint conditions in this study are still idealizations of the mechanical environment. For example, these simulations assume that joints are perfectly rigid, allowing no motion in constrained degrees-of-freedom. In reality, constraints are enforced by structures which have a finite stiffness. It may be possible to achieve a somewhat more realistic simulation by including bones in the foot and thigh, and simulating contact at the joints. However, this would add multiple sources of nonlinearity, greatly increasing complexity and computational time; such an approach may not be suitable for studies with a large number of participants. Finally, there may be errors associated with geometry and scaling of the MSK model. The original model geometry represents a 170 cm tall adult male [23], which is scaled based on measurement of weight and body segment length. We speculate that individuals may have important differences in bone shape that are not captured in this method of scaling; these differences could cause changes to muscle moment arms and calculations of muscle forces (Eq. (3)), though further investigation is required.

5 Conclusions

We used an integrative modeling approach, combining inverse dynamics, MSK modeling, and FE modeling to predict tibia deformation. Model complexity, i.e., BC and loading condition, had a large effect on FE predicted deformation angles. The most complex conditions predicted tibial deformation angles and shaft strains consistent with previous in vivo measurements. Thus, we believe this workflow is sufficiently realistic to be used to assess relative stress fracture risk. Furthermore, results of this study

suggest that changes to gait can cause large changes to tibia deformation, particularly in torsion. The workflow introduced here could be a powerful tool to study this phenomenon in the future.

Funding Data

- Natural Sciences and Engineering Research Council of Canada (WBE; RGPIN 01029-2015, Funder ID: 10.13039/501100002790).

References

- [1] Jones, B. H., Thacker, S. B., Gilchrist, J., Kimsey, C. D., and Sosin, D. M., 2002, "Prevention of Lower Extremity Stress Fractures in Athletes and Soldiers: A Systematic Review," *Epidemiol. Rev.*, **24**(2), pp. 228–247.
- [2] Matheson, G. O., Clement, D. B., McKenzie, D. C., Taunton, J. E., Lloyd-Smith, D. R., and Macintyre, J. G., 1987, "Stress Fractures in Athletes: A Study of 320 Cases," *Am. J. Sports Med.*, **15**(1), pp. 46–58.
- [3] Burr, D. B., 1997, "Bone, Exercise, and Stress Fractures," *Exerc. Sport Sci. Rev.*, **25**(1), pp. 171–94.
- [4] Brent Edwards, W., 2018, "Modeling Overuse Injuries in Sport as a Mechanical Fatigue Phenomenon," *Exerc. Sport Sci. Rev.*, **46**(4), pp. 224–231.
- [5] Zioupos, P., Wang, X. T., and Currey, J. D., 1996, "The Accumulation of Fatigue Microdamage in Human Cortical Bone of Two Different Ages In Vivo," *Clin. Biomech.*, **11**(7), pp. 365–375.
- [6] Carter, D. R., Caler, W. E., Spengler, D. M., and Frankel, V. H., 1981, "Fatigue Behavior of Adult Cortical Bone: The Influence of Mean Strain and Strain Range," *Acta Orthop.*, **52**(5), pp. 481–490.
- [7] Matcuk, G. R., Mahanty, S. R., Skalski, M. R., Patel, D. B., White, E. A., and Gottsegen, C. J., 2016, "Stress Fractures: Pathophysiology, Clinical Presentation, Imaging Features, and Treatment Options," *Emerg. Radiol.*, **23**(4), pp. 365–375.
- [8] Pattin, C. A., Caler, W. E., and Carter, D. R., 1996, "Cyclic Mechanical Property Degradation During Fatigue Loading of Cortical Bone," *J. Biomech.*, **29**(1), pp. 69–79.
- [9] Milgrom, C., Radeva-Petrova, D. R., Finestone, A., Nyska, M., Mendelson, S., Benjuya, N., Simkin, A., and Burr, D., 2007, "The Effect of Muscle Fatigue on In Vivo Tibial Strains," *J. Biomech.*, **40**(4), pp. 845–850.
- [10] Milgrom, C., Finestone, A., Levi, Y., Simkin, A., Ekenman, I., Mendelson, S., Millgram, M., Nyska, M., Benjuya, N., and Burr, D., 2000, "Do High Impact Exercises Produce Higher Tibial Strains Than Running?," *Br. J. Sports Med.*, **34**(3), pp. 195–199.
- [11] Milgrom, C., Finestone, A., Segev, S., Olin, C., Arndt, T., and Ekenman, I., 2003, "Are Overground or Treadmill Runners More Likely to Sustain Tibial Stress Fracture?," *Br. J. Sports Med.*, **37**(2), pp. 160–163.
- [12] Burr, D. B., Milgrom, C., Fyhr, D., Forwood, M., Nyska, M., Finestone, A., Hoshaw, S., Saig, E., and Simkin, A., 1996, "In Vivo Measurement of Human Tibial Strains During Vigorous Activity," *Bone*, **18**(5), pp. 405–410.
- [13] Lanyon, L. E., Hampson, W. G. J., Goodship, A. E., Shah, J. S., Hampson, W. G. J., Goodship, A. E., and Bone, J. S. S., 1975, "Bone Deformation Recorded In Vivo From Strain Gauges Attached to the Human Tibial Shaft," *Acta Orthop. Scand.*, **46**(2), pp. 256–268.
- [14] Yang, P. F., Sanno, M., Ganse, B., Koy, T., Brüggemann, G. P., Müller, L. P., and Rittweger, J., 2014, "Torsion and Antero-Posterior Bending in the In Vivo Human Tibia Loading Regimes During Walking and Running," *PLoS One*, **9**(4).
- [15] Haider, I. T., Schneider, P., Michalski, A., and Edwards, W. B., 2018, "Influence of Geometry on Proximal Femoral Shaft Strains: Implications for Atypical Femoral Fracture," *Bone*, **110**, pp. 295–303.
- [16] Edwards, W. B., Taylor, D., Rudolph, T. J., Gillette, J. C., and Derrick, T. R., 2010, "Effects of Running Speed on a Probabilistic Stress Fracture Model," *Clin. Biomech.*, **25**(4), pp. 372–377.
- [17] Edwards, W. B., Miller, R. H., and Derrick, T. R., 2016, "Femoral Strain During Walking Predicted With Muscle Forces From Static and Dynamic Optimization," *J. Biomech.*, **49**(7), pp. 1206–1213.
- [18] Xu, C., Silder, A., Zhang, J., Hughes, J., Unnikrishnan, G., Reifman, J., and Rakesh, V., 2016, "An Integrated Musculoskeletal-Finite-Element Model to Evaluate Effects of Load Carriage on the Tibia During Walking," *ASME J. Biomech. Eng.*, **138**(10), p. 101001.
- [19] Hadid, A., Epstein, Y., Shabshin, N., and Gefen, A., 2018, "Biomechanical Model for Stress Fracture-Related Factors in Athletes and Soldiers," *Med. Sci. Sport. Exerc.*, **50**(9), pp. 1827–1836.
- [20] Difo Kaze, A., Maas, S., Arnoux, P.-J., Wolf, C., and Pape, D., 2017, "A Finite Element Model of the Lower Limb During Stance Phase of Gait Cycle Including the Muscle Forces," *Biomed. Eng. Online*, **16**(1), p. 138.
- [21] Vaughan, C. L., Davis, B. L., and O'Connor, J. C., 1999, "Dynamics of Human Gait," *Dynamics of Human Gait*, Vol. 1, Human Kinetics Publishers, Cape Town, South Africa.
- [22] Boyer, E. R., and Derrick, T. R., 2018, "Lower Extremity Joint Loads in Habitual Rearfoot and Mid/Forefoot Strike Runners With Normal and Shortened Stride Lengths," *J. Sports Sci.*, **36**(5), pp. 499–505.
- [23] Arnold, E. M., Ward, S. R., Lieber, R. L., and Delp, S. L., 2010, "A Model of the Lower Limb for Analysis of Human Movement," *Ann. Biomed. Eng.*, **38**(2), pp. 269–279.

- [24] Edwards, W. B., Schnitzer, T. J., and Troy, K. L., 2013, "Torsional Stiffness and Strength of the Proximal Tibia Are Better Predicted by Finite Element Models Than DXA or QCT," *J. Biomech.*, **46**(10), pp. 1655–1662.
- [25] Dalstra, M., Huiskes, R., Odgaard, A., and van Erning, L., 1993, "Mechanical and Textural Properties of Pelvic Trabecular Bone," *J. Biomech.*, **26**(4–5), pp. 523–535.
- [26] Rho, J. Y., 1996, "An Ultrasonic Method for Measuring the Elastic Properties of Human Tibial Cortical and Cancellous Bone," *Ultrasonics*, **34**(8), pp. 777–783.
- [27] Speirs, A. D., Heller, M. O., Duda, G. N., and Taylor, W. R., 2007, "Physiologically Based Boundary Conditions in Finite Element Modelling," *J. Biomech.*, **40**(10), pp. 2318–23.
- [28] Zhao, D., Banks, S. A., D'Lima, D. D., Colwell, C. W., and Fregly, B. J., 2007, "In Vivo Medial and Lateral Tibial Loads During Dynamic and High Flexion Activities," *J. Orthop. Res.*, **25**(5), pp. 593–602.
- [29] Carrera, I., Gelber, P. E., Chary, G., Gomez Masdeu, M., González Ballester, M. A., Monllau, J. C., and Noailly, J., 2018, "An Intact Fibula May Contribute to Allow Early Weight Bearing in Surgically Treated Tibial Plateau Fractures," *Knee Surg., Sport. Traumatol. Arthrosc.*, **26**(3), pp. 756–761.
- [30] Burkhart, T. A., Asa, B., Payne, M. W. C., Johnson, M., Dunning, C. E., and Wilson, T. D., 2015, "Anatomy of the Proximal Tibiofibular Joint and Interosseous Membrane, and Their Contributions to Joint Kinematics in Below-Knee Amputations," *J. Anat.*, **226**(2), pp. 143–149.
- [31] Scott, J., Lee, H., Barsoum, W., and van den Bogert, A. J., 2007, "The Effect of Tibiofemoral Loading on Proximal Tibiofibular Joint Motion," *J. Anat.*, **211**(5), pp. 647–653.
- [32] Beumer, A., Hemert, W. L. W. V., Swierstra, B. A., Jasper, L. E., and Belkoff, S. M., 2003, "A Biomechanical Evaluation of the Tibio Bular and Tibiotalar Ligaments of the Ankle," *Foot Ankle Int.*, **24**(5), pp. 426–429.
- [33] Marchetti, D. C., Moatshe, G., Phelps, B. M., Dahl, K. D., Ferrari, M. B., Chahla, J., Turnbull, T. L., and LaPrade, R. F., 2017, "The Proximal Tibiofibular Joint: A Biomechanical Analysis of the Anterior and Posterior Ligamentous Complexes," *Am. J. Sports Med.*, **45**(8), pp. 1888–1892.
- [34] Lambert, K. L., 1971, "The Weight-Bearing Function of the Fibula. A Strain Gauge Study," *J. Bone Jt. Surg. Am.*, **53**(3), pp. 507–513.
- [35] Garijo, N., Verdonschot, N., Engelborghs, K., García-Aznar, J. M., and Pérez, M. A., 2017, "Subject-Specific Musculoskeletal Loading of the Tibia: Computational Load Estimation," *J. Mech. Behav. Biomed. Mater.*, **65**, pp. 334–343.
- [36] Firminger, C. R., Fung, A., Loundagin, L. L., and Edwards, W. B., 2017, "Effects of Footwear and Stride Length on Metatarsal Strains and Failure in Running," *Clin. Biomech.*, **49**, pp. 8–15.
- [37] Edwards, W. B., Taylor, D., Rudolph, T. J., Gillette, J. C., and Derrick, T. R., 2009, "Effects of Stride Length and Running Mileage on a Probabilistic Stress Fracture Model," *Med. Sci. Sports Exerc.*, **41**(12), pp. 2177–2184.
- [38] Milner, C. E., Davis, I. S., and Hamill, J., 2006, "Free Moment as a Predictor of Tibial Stress Fracture in Distance Runners," *J. Biomech.*, **39**(15), pp. 2819–2825.
- [39] Holden, J. P., and Cavanagh, P. R., 1991, "The Free Moment of Ground Reaction in Distance Running and Its Changes With Pronation," *J. Biomech.*, **24**(10), pp. 887–897.
- [40] Spector, F. C., Karlin, J. M., DeValentine, S., Scurran, B. L., and Silvani, S. L., 1983, "Spiral Fracture of the Distal Tibia: An Unusual Stress Fracture," *J. Foot Surg.*, **22**(4), pp. 358–61.
- [41] Dal, U., Erdogan, T., Resitoglu, B., and Beydagi, H., 2010, "Determination of Preferred Walking Speed on Treadmill May Lead to High Oxygen Cost on Treadmill Walking," *Gait Posture*, **31**(3), pp. 366–369.
- [42] Bergmann, G. (ed.), and Charité Universitätsmedizin Berlin, 2018, "Orthoload Database," Berlin, accessed Oct. 10, 2018, https://orthoload.com/entries:k11_180908;k2l_300908_1_19p;k3r_300908_1_27p;k5r_020210_1_59p;k7l_080611_1_31p;k8l_020210_2_128p.
- [43] Derrick, T. R., Edwards, W. B., Fellin, R. E., and Seay, J. F., 2016, "An Integrative Modeling Approach for the Efficient Estimation of Cross Sectional Tibial Stresses During Locomotion," *J. Biomech.*, **49**(3), pp. 429–435.